

# High-Resolution Photoluminescence Electro-Modulation Microscopy by Scanning Lock-In

W. Koopman<sup>1,a</sup>, M. Muccini<sup>2</sup> and S. Toffanin<sup>2,b</sup>

<sup>1</sup>*Institute of Physics and Astronomy, University of Potsdam, Karl-Liebknecht-Str. 24-25, Potsdam, 14476, Germany*

<sup>2</sup>*CNR-ISMN Bologna, Via P.Gobetti 101, 40129, Bologna (BO), Italy*

Morphological inhomogeneities and structural defects in organic semiconductors crucially determine the charge accumulation and lateral transport in organic thin-film transistors.

Photoluminescence Electro-Modulation (PLEM) microscopy is a laser-scanning microscopy technique that relies on the modulation of the thin-film fluorescence in the presence of charge carriers to image the spatial distribution of charges within the active organic semiconductor. Here, we present a lock-in scheme based on a scanning beam approach for increasing the PLEM microscopy resolution and contrast. The charge density in the device is modulated by a sinusoidal electrical signal, phase-locked to the scanning beam of the excitation laser. The lock-in detection scheme is achieved by acquiring a series of images with different phases between the beam scan and the electrical modulation. Application of high resolution PLEM to an organic transistor in accumulation mode demonstrates its potential to image local variations in the charge accumulation. A diffraction-limited precision of sub-300 nm and a signal to noise ratio of 21.4 dB could be achieved.

## I. INTRODUCTION

The electrical properties of organic transistors (OFETs) are largely determined by the distribution of charges in the nm-thick accumulation layer at the interface between the organic semiconductor (OSC) and the dielectric<sup>1-6</sup>. On a device scale, the location of charge accumulation, depletion and recombination zones crucially determine the basic working principles of OFETs<sup>2,7-9</sup>. On a microscopic scale, charge trapping at structural defects and impurities determine the electrical transport properties, like charge carrier mobility and device

---

<sup>a</sup> This research was performed while W. Koopman was at CNR-ISMN Bologna, Via P.Gobetti 101, 40129, Bologna (BO), Italy

<sup>b</sup> Author to whom correspondence should be addressed: [s.toffanin@bo.ismn.cr.it](mailto:s.toffanin@bo.ismn.cr.it)

resistance<sup>10–12</sup> as well as electroluminescence properties<sup>13</sup>. Experimental techniques that give direct access to the charge distribution are therefore highly capable tools for understanding and for optimizing the charge transport in OFETs<sup>14</sup>.

A plethora of techniques have been developed to obtain a direct microscopic spatial mapping of the electrostatics in OFETs<sup>14–18</sup>. The most advanced of these is scanning Kelvin-probe microscopy<sup>19</sup>, which senses the interaction of the local electrical potential with an AFM tip<sup>15,20–24</sup>. While this technique allows a direct measurement of the local potential and its correlation to morphological features, it is limited to surface measurements only. In particular, it cannot be used to study buried interfaces in multilayer devices or to access the area below metallic top contacts. Techniques based on optical probes<sup>14,16,18,25–28</sup> present an alternative that can access different layers individually, by taking advantage of the distinct optical properties of each layer<sup>29</sup>. Moreover, if transparent substrates are used, they can also reach areas below metal contacts to probe the mechanisms of charge injection. Approaches to probe the electrostatics of OFETs by optical probes are based on e.g. the dependence of non-linear optical effects on the local electrical field, like second harmonic generation<sup>14,25,26,30</sup> or the electrooptical Stark effect<sup>16,27</sup>, or the presence of polaron absorption features<sup>17</sup>. All these techniques have the drawback that they require extensive prior knowledge about the optical properties of the OSC under investigation and require a precise adjustment of the excitation conditions to each specific OSC. Moreover, they all suffer from very low signal strength, which renders high-resolution imaging to resolve charge accumulation spatial distribution at the micro-scale difficult or impossible.

Recently, we introduced Photoluminescence Electro-Modulation Microscopy (PLEM) as a technique that allows the direct mapping of the charge density distribution in OFETs<sup>18</sup>. The presence of charges is detected by the charge-induced quenching of excitons<sup>31</sup>. In short, the working principle of the PLEM technique is the following: a confocal laser-scanning microscope collects the photoluminescence (PL) from the semiconductor layer of an OFET, while the transistor is alternately switched between the biased (on-state) and in the unbiased state (off-state). Comparing the images collected in the on- and off-states yields a measurement of the local exciton-quenching due to charge-exciton interaction according to:

$$\eta(x, y) = \frac{PL_0(x, y) - PL_V(x, y)}{PL(x, y)} = \frac{\Delta PL}{PL_0} \quad (1)$$

Here  $PL_V$  denotes the PL from the semiconductor in on-state and  $PL_0$  the PL in the off-state.

The quantity  $\eta$  derived in this way is a measure for the charge density<sup>18,31,32</sup>.

PLEM was successfully used to map the charge accumulation and depletion regions in active OFETs<sup>18</sup>. However, the technique would be even more valuable, if the morphology-dependent details of the local charge accumulation distribution could be resolved with maximized signal-to-noise ratio (SNR), which was not possible with these already-reported measurements. As PLEM relies on the measurement of small differential signals, it is only effective if the ratio of quenched to generated excitons is higher than the noise fluctuations during the measurements.

However, the differences in the local charge accumulation are expected to be minute and moreover the smaller the spot from which the signal is detected, the lower is the ratio between PL quenching and noise fluctuations.

The main challenge for implementing a high-resolution PLEM-microscope is setting-up a suitable detection scheme. A lock-in scheme can be used to selectively amplify only the desired differential (quenching) signal, while rejecting noise and unwanted slowly varying background-signals. In such a lock-in scheme, the device is periodically charged (by an AC bias), which in turn leads to a periodic modulation of the PL quenching. Demodulation of the PL from the device then gives a high resolution PLEM signal. The lock-in scheme decreases the background noise in the image, which in turn enhances the SNR and peak-SNR (PSNR-ratio between highest signal and noise floor), the latter being a direct measure for the image contrast. Thus, while the lock-in does not increase the physical optical resolution, by increasing the contrast it increases the practical achievable resolution. As a side effect, such a scheme also prevents the unwanted “charging” of the device caused by a prolonged application of a DC bias to the device. The already-reported lock-in schemes developed for the use with confocal scanning microscopes implement a “pixel-by-pixel” approach<sup>14,16,26,27,30</sup>. The excitation beam then dwells for several modulation periods on one pixel. The integration time per pixel is determined by the desired filter bandwidth, which is expressed by the time-constant of the lock-in amplifier.

frequencies are limited by the device response – in particular, by the charge injection and the dielectric response of the gate dielectric – to a maximum of hundreds of Hertz<sup>33</sup>. For an acceptable filter bandwidth, long time-constants are therefore required. On the other hand, organic semiconductors are prone to photobleaching, which drastically limits the dwell time

per pixel. This is particularly true for PLEM, given that the organic active layer is excited at the resonant frequency. This effectively limits the possible pixel dwell time to several milliseconds.

In this article, we introduce a novel scanning lock-in technique that employs a free scanning beam with dwell times (that is the time the laser dwells on a single point of the sample) of a few microseconds. It relies on coupling a modulation voltage in the temporal domain to a modulation of the PLEM image in the spatial domain and on the repetitive acquisition of the same image. The lock-in is realized as full software solution and can be implemented with any laser scanning microscope, home build or commercial that provides a synchronization signal to synchronize the modulation signal and beam scanning. We demonstrate the ability of this technique to obtain detailed images of the microscopic charge accumulation, with a diffraction limited resolution of sub 300 nm. While this lock-in scheme was developed explicitly for PLEM-microscopy, it is not limited to this technique and can in principle be implemented with other laser scanning microscopy techniques as well.

## II. LOCK-IN SCANNING MICROSCOPE

### A. Principle

The idea at the basis of the scanning lock-in scheme presented here, is to establish a link between a temporal modulation of a sample property, in case of PLEM technique the charge density distribution, and the spatial position of the free scanning beam. Instead of dwelling on one pixel for many periods of the reference signal and then moving to the next pixel, the beam is continuously scanned across the sample in lines and the modulation voltage is synchronized to the line scans. This approach reduces the necessary dwell-time per pixel to several microseconds and hence reduces the thermal stress on the OSC.

The principle is demonstrated in Figure 1. The scanning of the laser beam (x-direction) and the periodic bias modulation are synchronized. This is, the bias modulation applied within every line is identical and no variation arises in y-direction. Along the scanning direction a periodic spatial pattern is imposed on the confocal image (Figure 1b), whose period is given by  $v_{scan}/\omega$ , where  $v_{scan}$  is the beam scanning speed and  $\omega$  the bias modulation period. In this way, the bias modulation applied to the sample in the temporal domain is effectively converted into a modulation of the collected image in the spatial domain.

A lock-in detection scheme can now be achieved by taking a stack of images with different phases of the modulation relative to the line scanning. Between the images (or planes) of the stack, the modulation signal is shifted by a phase  $\varphi$ . If  $\varphi$  is chosen such that the corresponding spatial shift is exactly one pixel, the intensity of the collected PL signal varies with the same spatial frequency in  $z$ -direction (between the planes) as it does in  $x$ -direction (in one line). In the case of using the PLEM microscopy in OFETs, the signal modulation is realized by applying an AC bias to the gate electrode. In mathematical terms, this modulation voltage is:

$$V = V_0 \cdot \sin(\omega_x x + \varphi(z)) + V_{DC} = V_0 \cdot \sin(\omega(x + z)) + V_{DC} \quad (2)$$

Here  $\omega = \omega_x$  is the modulation frequency in  $x$ -direction and  $\varphi(z) = \omega z$  the total phase shift for the  $z^{\text{th}}$  image. As PLEM microscopy measures the difference between the biased and the unbiased device, the modulation bias must start from  $0$  V up to the desired quenching bias. Therefore,  $V_0 = V_g/2$ , while  $V_{DC} = V_0$  presents an additional DC-component that ensures a modulation bias starting from zero.

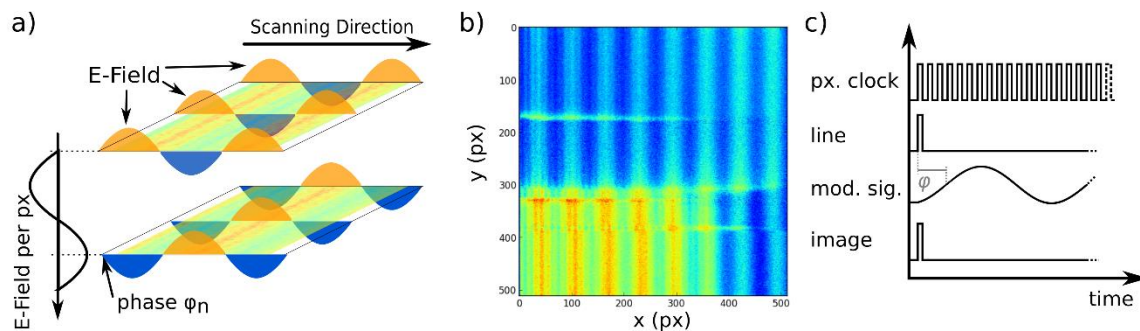


**Figure 1:** The scanning lock-in modulates the charge density of an OFET by periodically varying  $V_g$ , synchronized to the beam scanning across the sample. The modulation waveform is phase-shifted between the individual images with  $\varphi$ . (a) The individual images show a spatially modulated PL signal (b). Lock-in detection takes place for each individual pixel across an image stack. The number of acquired images in the stack determines the lock-in bandwidth. (c) Synchronization scheme for pixel clock, line scan, modulation signal and image scan. The phase  $\varphi$  of the modulation signal is shifted between the images.

Each measurement now corresponds to a 3D image stack, modulated in the  $x$ - and  $z$ -directions. The basic principle of a lock-in amplifier is to perform a Fourier analysis of a modulated measurement and select only the components at the modulation frequency. We achieved this by multiplying each image in  $x$ -direction (line-wise) with a reference signal and subsequently averaging each pixel along the  $z$ -direction. The procedure is possible, because of the coupling between the corresponding modulations in the  $x$ - and in  $z$ -directions. The integration period is not given by the dwell time on each individual picture but accordingly defined by the number of collected images.

The advantage of applying an AC bias to each line instead of changing the applied bias between the collected images, is that in the former case a buildup of a permanent charge between the image acquisitions is prevented. If a DC bias were applied during an entire image acquisition period, either a long waiting time in the range of minutes should be necessary after each image to deplete the OFET, or the transistor would not be depleted between the subsequent image acquisitions. By means of the lock-in scheme that we propose we avoid a massive residual charge in the device that would cause different PLEM signals between two subsequent images even though the same bias conditions were applied. Applying an AC bias instead periodically depletes the transistor and no differences in subsequent images were found.

## **B. Implementation**

Our setup is based on an inverted microscope (Nikon TE2000) equipped with a commercial confocal scanning module (Nikon EZ-C1). The scanning lock-in microscope can however be implemented with every laser scanning apparatus that offers suitable synchronization signals. A sketch of the principle setup is given in Figure 2. As excitation source, we use the second harmonic (488nm) of a MHz femtosecond oscillator (Spectra-Physics Tsunami), which allows high excitation densities while reducing the thermal stress on the sample. This specific excitation is not a principle requirement for the scanning lock-in, though. Before entering the scanning head, the laser was mode-cleaned by a spatial filter to ensure a Gaussian beam profile. The confocal scanning head mainly consisted of three crucial elements: a scanning mirror is used to scan the excitation beam across the sample through an objective and to collect the PL from the same spot. A dichroic mirror then separates the back-reflected PL from the excitation beam. Finally, the PL is routed through a pinhole in a confocal configuration, which rejects out-of-plane contributions from material above and beneath the focal plane.

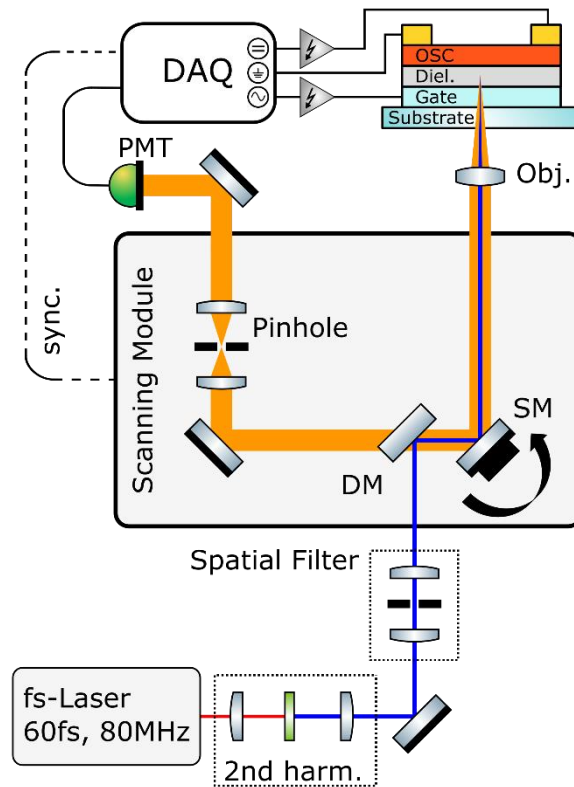


**Figure 2:** Sketch of the experimental apparatus. The OSC layer of an OFET is excited by the 2<sup>nd</sup> harmonic of a fs-oscillator. A scanning mirror (SM) scans the excitation beam across the sample through an objective (60x, NA 0.7) and collects PL from the same spot. A dichroic mirror (DM) separates the PL from the excitation, which is subsequently fed through a pinhole in a confocal configuration and collected by a PMT. Analogue PMT signal and TTL synchronization lines are recorded by the data acquisition board (DAQ), which also generates a modulated gate voltage and a constant drain voltage. The source electrode is connected to the ground of the DAQ.

The scanning lock-in is realized as full software solution (National Instruments LabView version 2013). A digital data acquisition (DAQ) module (National Instruments USB-6356) is employed for signal generation, data acquisition and synchronization to the confocal scanning-head. Two analogue outputs of the DAQ module provide a constant DC and a square wave AC-voltage. The AC-voltage is the modulation signal for the lock-in measurement. The phase  $\varphi_n$  of the AC waveform of the  $n^{\text{th}}$  image relative to the start of a line-scan is:

$$\varphi_n = n \cdot 2\pi/N \quad (3)$$

Here  $N$  is the total number of images taken. Between two successive images the phase must be increased such that it causes a shift of the modulation larger than one pixel. Otherwise the modulation of both images is identical. After every line-scan the AC waveform is restarted and

synchronized to the start of the next scan. During OFET-measurements, the AC-signal is applied to the gate electrode, such that it modulates the charge-density with time, while a constant bias is applied as drain-source voltage. A potential amplifier allows to apply voltages up to 120 V with a precision of nominal 30  $\mu$ V.

After passing through the confocal scanning head, the fluorescence intensity of every individual point is recovered by a home-build photo-multiplier-tube (PMT) module based on a Hamamatsu R-928 PMT. The PMT-signal is subsequently fed into an analogue input channel of the DAQ module and converted into a 16-bit digital signal. The PMT-bias and sensitivity of the DAQ input determine the maximum dynamic-range obtainable.

In order to synchronize the DAQ to the scanner, the position controller of the scanning mirror generates three digital TTL-signals (Figure 1c). The first channel (pixel clock) indicates a step in the horizontal or x-direction and the second (line trigger) a step in the vertical or y-direction. The third channel (image trigger) finally signalizes the end of an image acquisition. All three channels are recorded by the digital inputs of the DAQ and utilized as trigger signals for the generation of the modulation signal and for image reproduction. The pixel clock initiates the recording of the PL intensity from the single pixel at the current position of the mirror. The image is then reconstructed pixel by pixel and after each line-scan the line-trigger initiates new line of the digital image. Simultaneously, at the start of every new line, the waveform generation of the AC signal is restarted. This is necessary as the repositioning of the mirror for scanning a new line would otherwise de-synchronize the AC-signal from the scanning. By resetting the waveform generation, the AC signal remained in synch with every line-scan.

The individual images with 1024 x 1024 px and 16 bit grey-scale resolution have a size of 2 MB each. For a good measurement, approximately 5000 steps are needed and at least 5 images per step should be stored. Thus, the total amount of data per measurement would be in the order of 50 GB, if the individual images of every step were stored. This is not an acceptable amount of data, even with huge storage capabilities in the range of some TB available nowadays. To reduce the amount of necessary data, a running averaging algorithm is implemented, adding the  $n^{\text{th}}$  image  $I_{n0}$  to the average of all preceding images  $I_{n-1}$  according to:

$$I_n = \frac{1}{n} I_{n0} + \frac{n-1}{n} I_{n-1} \quad (4)$$

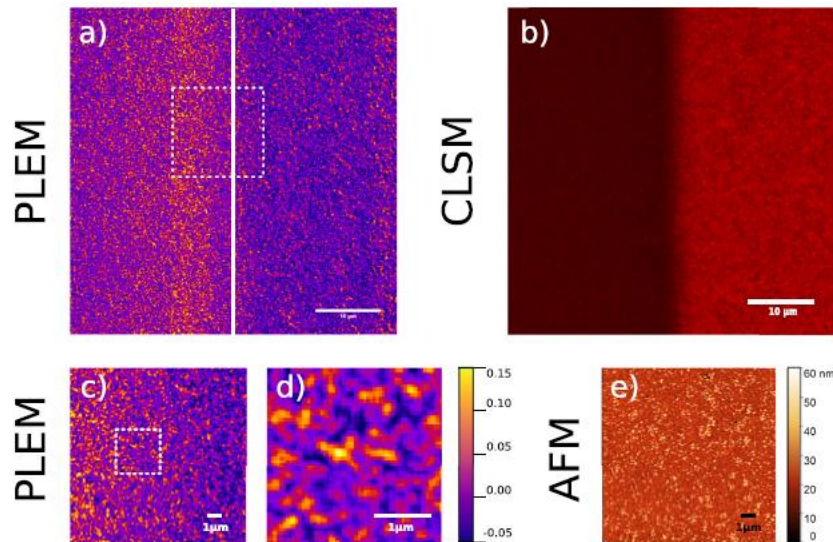
Here  $I_n$  is the average of  $n$  images. The software could produce three types of images: a simple average of all images, an image of the PLEM signal and an image the phase between the measured and the reference signal.

### III. MEASURING LOCAL CHARGE DISTRIBUTION IN OFETS

To demonstrate the capabilities of the scanning lock-in PLEM microscope, we demonstrate in the following its application for performing high-resolution imaging of the metal/organic interface of a biased OFET. The images were taken from an OFET based on the organic small molecule semiconductor (2,20-(2,20-bithiophene-5,50-diyl)bis(5-butyl-5H-thieno[2,3-c]pyrrole-4,6)-dione (NT4T)<sup>34,35</sup> a prototypical member of the highly versatile thiophene OSC family<sup>36,37</sup>, whose properties are representative of the entire organic semiconductor materials class.

The electro-modulation images were acquired using a 60x objective (Nikon Plan Fluor ELWD 60x air) and a pinhole with a size of 5  $\mu\text{m}$  was employed. The integration time per pixel was set to 3  $\mu\text{s}$ . The images were taken at a modulation frequency of 100 Hz. For this modulation frequency, the phase shift was set to 10 pixels, which results in 35 steps for one cycle. At each voltage, the image was averaged over 150 cycles, which equals a total of 5250 images.

The detection scheme discussed here requires that the sample is stable during the entire course of the measurement. Even though the lock-in scheme can filter a slow decrease of the quenching signal, a permanent degeneration of the semiconductor might also lead to changes in the electrical transistor behavior. We used samples that were encapsulated after fabrication in a nitrogen atmosphere. An alternative approach would be to perform all measurements in vacuum conditions. Degeneration of the sample during the measurement was monitored by comparing confocal fluorescence images taken before and after the PLEM-measurement. No difference in PL intensity could be measured.



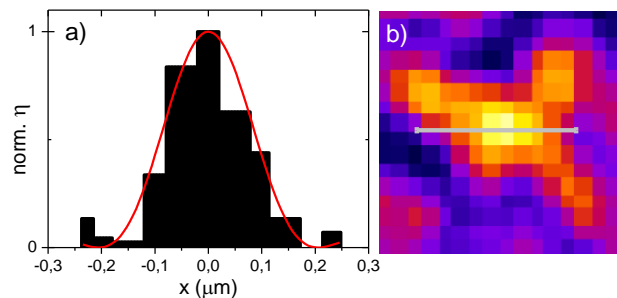
**Figure 3:** High resolution PLEM image of N4TN semiconducting layer in charge accumulation mode (a). The metal/organic region is located to the right of the white line. Charge accumulation at individual grains is clearly visible. Detail images (c, d) taken from the regions marked with dashes. (b) Confocal fluorescence image (without quenching) form the same region for comparison. (e) AFM image of NT4T semiconductor surface morphology.

Figure 3 presents high resolution PLEM image of the organic active layer underneath the metal electrode in pure charge accumulation, with a gate bias peak-to-peak amplitude of  $V_g = 100$  V and a vanishing drain-source bias. The images clearly show the pseudo morphological details of the charge accumulation at sub-micrometer structures.

The optical resolution of a microscope can be obtained by measuring the apparent size of a sub-diffraction limited scattered, such as a nanoparticle. As PLEM relies on the electromodulation of thin films, this approach is not feasible to determine the resolution in this case.

We therefore estimated the microscope resolution by measuring the apparent size of one of a small nanostructure (Figure 4a). The resolution obtained this way gives the minimum resolution of the microscope. A comparison of the size of the observed nanostructures with the theoretical resolution limit in confocal optical microscopy shows that the resolution of the collected PLEM images is diffraction-limited (Figure 4b). Quantitatively, the calculated resolution depends on the definition used. The FWHM of the structure is 140nm, while the distance between the two first minima is 400 nm. The widely used Rayleigh criterium defines the resolution as distance between the zero order maximum and the first minimum on one side. According to this criterium the resolution is about 200 nm.

In Figure 3c, we report an AFM image of the active layer of the NT4N base device <sup>34</sup>. By comparing same length-scale images reported in Figure 3c and 3d, it can be observed that the grain-like textures of the topographical image and of the in-plane distribution of PLEM intensity are similar in domain dimensions and distribution. This similarity suggests that the local differences in the charge density observed by PLEM microscopy might be correlated to individual grains of the polycrystalline OSC. Possibly, a different molecular orientation within different crystalline domains could be responsible for the observed spatial distribution of the charge density. Indeed, it is likely that the sub-micrometric regions that are bright yellow in the PLEM image (i.e. regions where intense exciton-charge quenching is observed, and eventually higher charge density is located) correspond to only those crystalline domains that are suitably oriented in the NT4N thin-film to enable effective lateral charge transport.



**Figure 4:** Comparison of feature size of PLEM images to diffraction limit (a) shows a resolution at the theoretical limit of sub 300 nm; (b) location of cross-section presented in (a).

As figures of merit for image quality obtained in our setup we determined the noise in a typical PLEM image and related it to: a) the medium (SNR) and b) the highest (image contrast or PSNR) signal in the image. In these calculations we used the actual pixel values (16 bit – from 0 to 65535) instead of the PLEM scale. The former is an absolute positive scale, while the latter allows for positive and negative values, which complicates the correct determination of the noise in the actual image (which can only have positive values). To separate the high-frequency noise from the low frequency image structures the image was filtered by a high pass FFT-filter. Subsequently, the standard deviation  $\sigma_{NOISE}$  of the noise was calculated as the standard deviation of the pixel values of the filtered image (figure 5).

With a standard deviation of  $\sigma_{NOISE} = 861.15$  px we calculated a SNR of 24.44 dB and an image contrast (PSNR) of 37.59 dB (Details of the calculation given in Appendix B).

According to the industry standard ISO 12232:2006 a contrast of 30 dB or more corresponds to an excellent image quality<sup>38</sup>. Moreover, the noise suppression of the lock-in scanning microscope discussed here is comparable to the suppression in commercial digital lock-in amplifiers. The image quality might be enhanced even further by increasing the number of modulation cycles for a further reduction of the noise floor. A theoretical limit at about 100 dB for the obtainable dynamic range is given by the 16-bit digitalization of the DAQ.

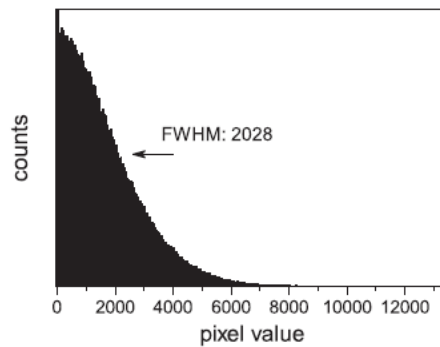


**Figure 5:** Histogram of noise measurement. The gaussian full-width half-maximum of 2028 px corresponds to a standard deviation of  $\sigma = \text{FWHM}/2.355 = 861.15$  px.

#### IV. CONCLUSIONS

In conclusion, we presented a new lock-in scanning technique for achieving high resolution PLEM images of the charge accumulation distribution in organic field-effect devices. This technique enables a sensitive electro-modulation sampling imaging without sample degradation in optical scanning microscope technique. PLEM measures the exciton quenching due to exciton-charge interaction, which is directly related to the local charge density. By implementing the reported scanning lock-in scheme in the PLEM microscopy, high resolution in planar organic field-effect devices can be obtained without stressing the device active layer even in the case of low-emissive organic semiconductors. Direct comparison of the PLEM mapping with other scanning probe techniques (i.e. CLSM and AFM) can be easily performed. The lock-in detection scheme here presented implements the coupling between the spatial scanning of the exciting laser beam and the periodic temporal modulation of the charge density in the device. The lock-in effect is then achieved by acquiring a stack of images with different phase-factors between the beam scanning and the electrical modulation. As an example of the capabilities of high-resolution PLEM, we demonstrated the imaging of the local charge distribution in an OFET. Details of the microscopic charge accumulation are visible with a diffraction limited resolution less than 300 nm. The image contrast (peak signal-to-noise-ratio)

of a test image taken with the lock-in was around 37.59 dB, while its signal-to-noise ratio was 24.44 dB: these values are both comparable with modern lock-in amplifiers.

In general, the versatility and high-sensitivity of this imaging technique enables direct access to different charge-mediated photophysical processes taking place at the same time in the active region of multifunctional field-effect devices, such as photoluminescence, electroluminescence, photocurrent and charge-injection/generation.

## ACKNOWLEDGMENTS

This work received funding from the European Union's Horizon 2020 research and innovation program under Grant Agreement No. 644742 (LEO Project) and No. 780839 (MOLOKO Project). We kindly acknowledge EU FP7 Marie Curie No. ITN-316832 project OLIMPIA and Fabbrica del Futuro: SILK.IT for financial support. Finally, we are grateful to M. Melucci from CNR-ISOF for providing NT4N material and F. Prescimone, V. Ragona, P. Mei, and T. Bonfiglioli from CNR-ISMN and Giovanni P. Donati for valuable technical contributions.

## APPENDIX A: DIFFRACTION SPOT CALCULATION

The diffraction limited spot was calculated according to <sup>30</sup>:

$$I(u) = \left[ \frac{\sin(u)}{u} \right]^2$$

Here  $u$  is a normalized coordinate that considers the influence of the wavelength,  $\lambda$ , and the numerical aperture,  $\alpha$ . It is related to the physical coordinate  $x$  by:

$$u(x) = \frac{1}{2} \cdot \frac{8\pi}{\lambda} \cdot \sin^2(\alpha) \cdot x$$

The FWHM and minima position of a sinc-function cannot be obtained in a closed analytical form. We therefore obtained these values for the sinc-function in figure 4a numerically. In the calculation of  $u(x)$  we used a wavelength of  $\lambda = 380 \text{ nm}$  and a numerical aperture of  $\alpha = 0.7$

## APPENDIX B: DYNAMIC RANGE AND SIGNAL-TO-NOISE

Two figures of merit were calculated to assess the image quality obtained by our setup. The image contrast or peak signal-to-noise ratio (PSNR) of an individual PLEM image is the ratio

of the highest signal  $\eta_{peak}$  in the image to the standard deviation  $\sigma_{noise}$  of the noise floor. The signal-to-noise ratio (SNR) of an image is given by the ratio of the average signal  $\eta_{av}$  to  $\sigma_{noise}$ .  $\eta_{av}$  was calculated as weighted mean of the pixel values (Figure 6). For the image presented in figure 3a, we calculated:

$$PSNR = 20 \cdot \log_{10} \left( \frac{\eta_{peak}}{\sigma_{noise}} \right) = 20 \log_{10} \left( \frac{65279}{861.15} \right) = 37.59 \text{ dB}$$

$$SNR = 20 \cdot \log_{10} \left( \frac{\eta_{av}}{\sigma_{noise}} \right) = 20 \log_{10} \left( \frac{14352}{2018} \right) = 24.44 \text{ dB}$$

All values are given as decadic logarithm of the ratio. The prefactor 20 was used in accordance to the recommendations in ISO 80000-1:2009 Annex. C on logarithmic quantities<sup>40</sup> and ISO 12232:2006 on photography and image quality<sup>38</sup>.

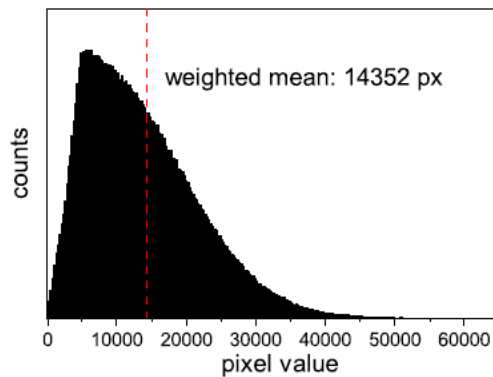


**Figure 6:** Histogram of pixel values in figure 3a. The weighted mean is at  $\eta_{av} = 14352$  px.

## REFERENCES

1. Z. Bao and J. J. Locklin, *Organic field-effect transistors* (CRC Press, Boca Raton, FL, 2007).
2. G. Horowitz, "Organic Field-Effect Transistors," *Advanced Materials* **10** (5), 365–377 (1998).
3. M. Muccini, W. Koopman, and S. Toffanin, "The photonic perspective of organic light emitting transistors," *Laser & Photon. Rev.* **6** (2), 258–275 (2012).
4. F. Todescato, R. Capelli, F. Dinelli, M. Murgia, N. Camaioni, M. Yang, R. Bozio, and M. Muccini, "Correlation between dielectric/organic interface properties and key electrical parameters in PPV-based OFETs," *The Journal of Physical Chemistry B* **112** (33), 10130–10136 (2008).
5. M. Muccini, "A bright future for organic field-effect transistors," *Nature Materials* **5** (8), 605–613 (2006).
6. P. Lutsyk, K. Janus, J. Sworakowski, G. Generali, R. Capelli, and M. Muccini, "Photoswitching of an n-Type Organic Field Effect Transistor by a Reversible Photochromic Reaction in the Dielectric Film," *J. Phys. Chem. C* **115** (7), 3106–3111 (2011).
7. G. Horowitz, P. Lang, M. Mottaghi, and H. Aubin, "Extracting Parameters from the Current-Voltage Characteristics of Organic Field-Effect Transistors," *Adv. Funct. Mater.* **14** (11), 1069–1074 (2004).

8. S. Toffanin, R. Capelli, W. Koopman, G. Generali, S. Cavallini, A. Stefani, D. Saguatti, G. Ruani, and M. Muccini, "Organic light-emitting transistors with voltage-tunable lit area and full channel illumination," *Laser & Photon. Rev.* **7** (6), 1011–1019 (2013).
9. H. L. Gomes, P. Stallinga, F. Dinelli, M. Murgia, F. Biscarini, D. M. de Leeuw, M. Muccini, and K. Müllen, "Electrical characterization of organic based transistors. Stability issues," *Polym. Adv. Technol.* **16** (2-3), 227–231 (2005).
10. A. A. Virkar, S. Mannsfeld, Z. Bao, and N. Stingelin, "Organic semiconductor growth and morphology considerations for organic thin-film transistors," *Advanced materials (Deerfield Beach, Fla.)* **22** (34), 3857–3875 (2010).
11. F. Liscio, C. Albonetti, K. Broch, A. Shehu, S. D. Quiroga, L. Ferlauto, C. Frank, S. Kowarik, R. Nervo, A. Gerlach, S. Milita, F. Schreiber, and F. Biscarini, "Molecular reorganization in organic field-effect transistors and its effect on two-dimensional charge transport pathways," *ACS nano* **7** (2), 1257–1264 (2013).
12. F. Dinelli, M. Murgia, P. Levy, M. Cavallini, F. Biscarini, and de Leeuw, Dago M., "Spatially Correlated Charge Transport in Organic Thin Film Transistors," *Physical Review Letters* **92** (11), 116802 (2004).
13. R. Capelli, S. Toffanin, G. Generali, H. Usta, A. Facchetti, and M. Muccini, "Organic light-emitting transistors with an efficiency that outperforms the equivalent light-emitting diodes," *Nature Materials* **9** (6), 496–503 (2010).
14. T. Manaka, E. Lim, R. Tamura, and M. Iwamoto, "Direct imaging of carrier motion in organic transistors by optical second-harmonic generation," *Nature Photonics* **1** (10), 581–584 (2007).
15. V. Palermo, M. Palma, and P. Samori, "Electronic Characterization of Organic Thin Films by Kelvin Probe Force Microscopy," *Advanced Materials* **18** (2), 145–164 (2006).
16. M. Celebrano, C. Sciascia, G. Cerullo, M. Zavelani-Rossi, G. Lanzani, and J. R. Cabanillas-Gonzalez, "Imaging the Electric-Field Distribution in Organic Devices by Confocal Electroreflectance Microscopy," *Adv. Funct. Mater.* **19** (8), 1180–1185 (2009).
17. C. Sciascia, N. Martino, T. Schuettfort, B. Watts, G. Grancini, M. R. Antognazza, M. Zavelani-Rossi, C. R. McNeill, and M. Caironi, "Sub-Micrometer Charge Modulation Microscopy of a High Mobility Polymeric n-Channel Field-Effect Transistor," *Advanced Materials* **23** (43), 5086–5090 (2011).
18. W. Koopman, S. Toffanin, M. Natali, S. Troisi, R. Capelli, V. Biondo, A. Stefani, and M. Muccini, "Mapping of charge distribution in organic field-effect transistors by confocal photoluminescence electromodulation microscopy," *Nano letters* **14** (4), 1695–1700 (2014).
19. S. Sadewasser and T. Glatzel, eds., *Kelvin Probe Force Microscopy. Measuring and Compensating Electrostatic Forces* (Springer-Verlag Berlin Heidelberg, Berlin, Heidelberg, 2012).
20. S. G.J. Mathijssen, M. Cölle, A. J.G. Mank, M. Kemerink, P. A. Bobbert, and de Leeuw, Dago M., "Scanning Kelvin probe microscopy on organic field-effect transistors during gate bias stress," *Applied Physics Letters* **90** (19), 192104 (2007).
21. D. Charrier, *Potentiometry on organic semiconductor devices*, Technische Universiteit Eindhoven, 2009.
22. Charrier, Dimitri S H, M. Kemerink, B. E. Smalbrugge, T. de Vries, and Janssen, René a J, "Real versus measured surface potentials in scanning Kelvin probe microscopy," *ACS nano* **2** (4), 622–626 (2008).
23. M. Kemerink, Charrier, Dimitri S H, E. C.P. Smits, S. G.J. Mathijssen, de Leeuw, Dago M., and Janssen, René a J, "On the width of the recombination zone in ambipolar organic field effect transistors," *Applied Physics Letters* **93** (3), 33312 (2008).
24. J. a. Nichols, D. J. Gundlach, and T. N. Jackson, "Potential imaging of pentacene organic thin-film transistors," *Applied Physics Letters* **83** (12), 2366–2368 (2003).

25. T. Manaka, E. Lim, M. Iwamoto, H. Kohn, and Y. Ohshima, "Direct observation of trapped carriers in polydiacetylene films by optical second harmonic generation," *Applied Physics Letters* **90** (17), 171119 (2007).
26. T. Manaka, E. Lim, R. Tamura, and M. Iwamoto, "Modulation in optical second harmonic generation signal from channel of pentacene field effect transistors during device operation," *Applied Physics Letters* **87** (22), 222107 (2005).
27. C. Sciascia, M. Celebrano, M. Binda, D. Natali, G. Lanzani, and J. R. Cabanillas-Gonzalez, "Electric field and charge distribution imaging with sub-micron resolution in an organic Thin-Film Transistor," *Organic Electronics* **13** (1), 66–70 (2012).
28. M. A. Loi, E. D. Como, F. Dinelli, M. Murgia, R. Zamboni, F. Biscarini, M. Muccini, and E. Da Como, "Supramolecular organization in ultra-thin films of  $\alpha$ -sexithiophene on silicon dioxide // Supramolecular organization in ultra-thin films of  $\alpha$ -sexithiophene on silicon dioxide," *Nature Materials* **4** (1), 81–85 (2004).
29. P. Mei, M. Murgia, C. Taliani, E. Lunedei, and M. Muccini, "Luminescence quantum yield of molecular aggregates and excitons in  $\alpha$ -sexithienyl thin films at variable temperature," *Journal of Applied Physics* **88** (9), 5158 (2000).
30. T. Manaka, E. Lim, R. Tamura, D. Yamada, and M. Iwamoto, "Probing of the electric field distribution in organic field effect transistor channel by microscopic second harmonic generation," *Applied Physics Letters* **89** (7), 72113 (2006).
31. W. Koopman, M. Natali, G. P. Donati, M. Muccini, and S. Toffanin, *Exciton-quenching by charges in organic field-effect devices with high-density space-charge regions*, 2015.
32. W. Koopman, *Excitons in Active Organic Devices*, Dissertation, RWTH Aachen University, 2014.
33. J. Veres, S. Ogier, G. Lloyd, and D. de Leeuw, "Gate Insulators in Organic Field-Effect Transistors," *Chem. Mater.* **16** (23), 4543–4555 (2004).
34. M. Melucci, L. Favaretto, M. Zambianchi, M. Durso, M. Gazzano, A. Zanelli, M. Monari, M. G. Lobello, F. de Angelis, V. Biondo, G. Generali, S. Troisi, W. Koopman, S. Toffanin, R. Capelli, and M. Muccini, "Molecular Tailoring of New Thieno(bis)imide- Based Semiconductors for Single Layer Ambipolar Light Emitting Transistors," *Chemistry of Materials* **25** (5), 668–676 (2013).
35. M. Melucci, M. Zambianchi, L. Favaretto, M. Gazzano, A. Zanelli, M. Monari, R. Capelli, S. Troisi, S. Toffanin, and M. Muccini, "Thienopyrrolyl dione end-capped oligothiophene ambipolar semiconductors for thin film- and light emitting transistors," *Chem. Commun. (Camb.)* **47** (43), 11840–11842 (2011).
36. T. Benincori, M. Capaccio, F. de Angelis, L. Falciola, M. Muccini, P. Mussini, A. Ponti, S. Toffanin, P. Traldi, and F. Sannicolò, "Spider-Like Oligothiophenes," *Chemistry - A European Journal* **14** (2), 459–471 (2008).
37. I. F. Perepichka and D. F. Perepichka, eds., *Handbook of Thiophene-based Materials*, 1<sup>st</sup> (John Wiley & Sons Ltd, Chichester, 2009).
38. International Organization for Standardization, *Photography—Digital still cameras—Determination of exposure index, ISO speed ratings, standard output sensitivity, and recommended exposure index*, 2006<sup>th</sup> ed. **37.040.10** (ISO 12232) (2006).
39. T. Wilson, *Confocal Microscopy*, 1<sup>st</sup> (Academic Press Limited, Oxford, 1990).
40. International Organization for Standardization, *Quantities and units—Part 1: General*, 2009 ed. **01.060** (ISO 80000-1) (2009).